Electronic Supplementary Material (ESI) for Inorganic Chemistry Frontiers.

Anisotropic X-ray Photovoltaics in 2D Trilayered Hybrid Perovskite $EA_4Pb_3Br_{10}$ Single Crystals with Low Detection Limit

Kewen Tao[a], Chenwei Xiong[b], Hui Yang[a], Hao Lin[b], Decai Ma[b], Huashan Li[a], Shaopeng Lin[b,*] and Biao Wang[a,**]

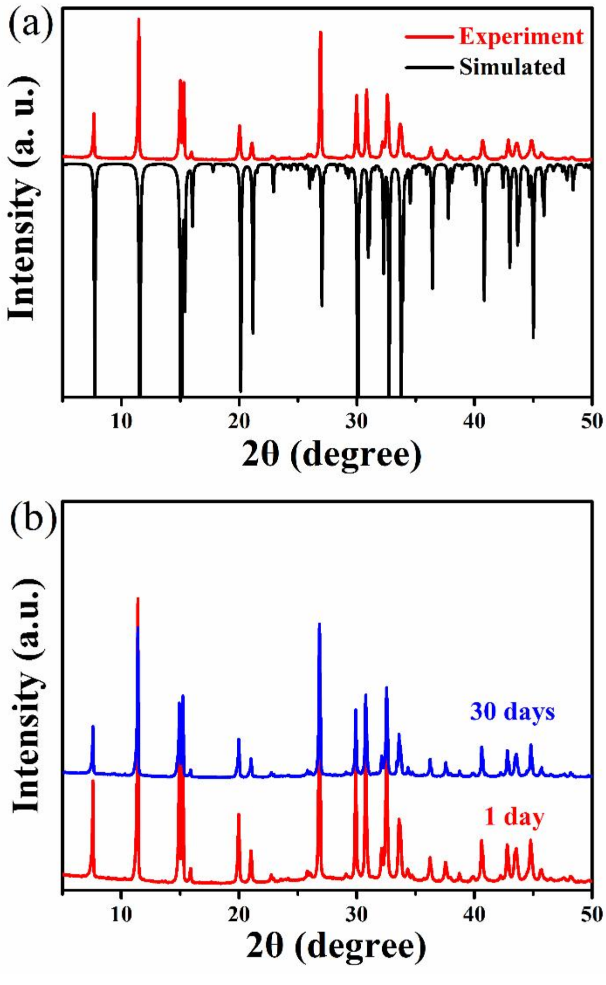

Fig. S1. a) Experiment and Simulated powder X-ray diffraction patterns of $EA_4Pb_3Br_{10}$. b) Powder X-ray patterns of $EA_4Pb_3Br_{10}$ recorded on the freshly-prepared sample (1 day) and after 30 days.

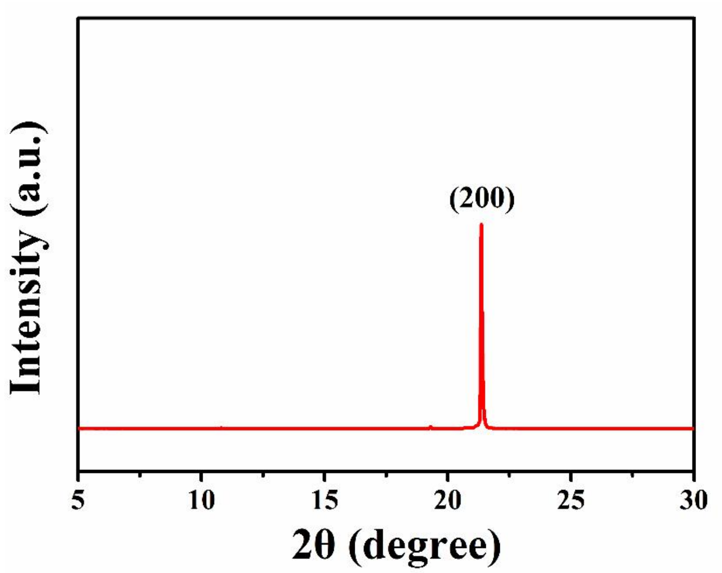

Fig. S2. XRD pattern of $EA_4Pb_3Br_{10}$ SC with the (h00) diffraction indices.

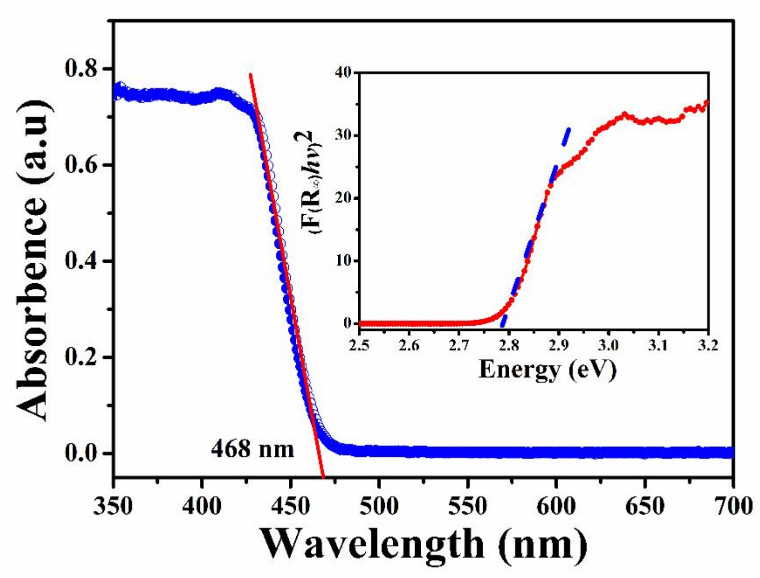

Fig. S3. UV–vis absorption spectrum of $EA_4Pb_3Br_{10}$. Insert: estimated bandgap.

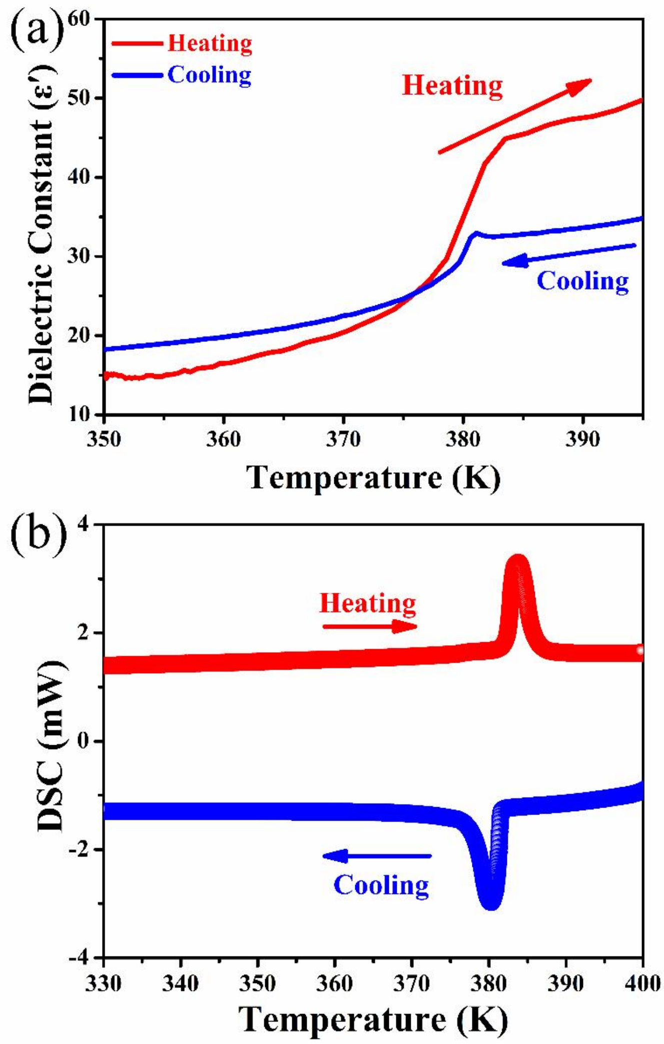

Fig. S4. a) Temperature-dependent dielectric constants (ε') of $EA_4Pb_3Br_{10}$ along the *a*-axis directions measured at 300 kHz. b) The DSC curves of $EA_4Pb_3Br_{10}$.

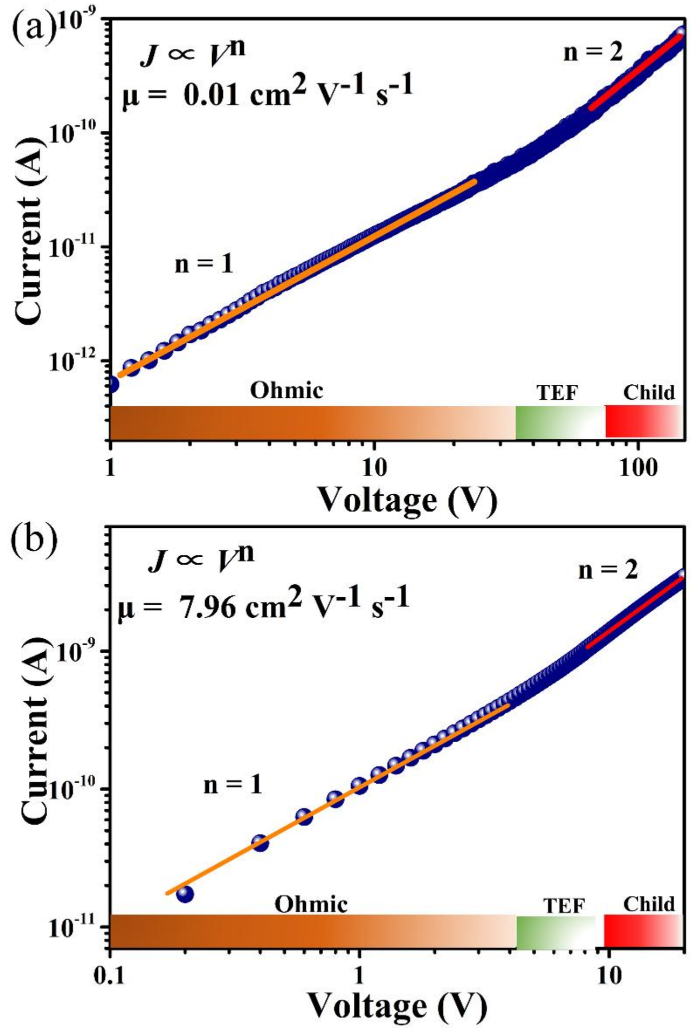

Fig. S5. Dark *I–V* curve along a) *b*-axis and b) *c*-axis of $EA_4Pb_3Br_{10}$ SC for SCLC analysis.

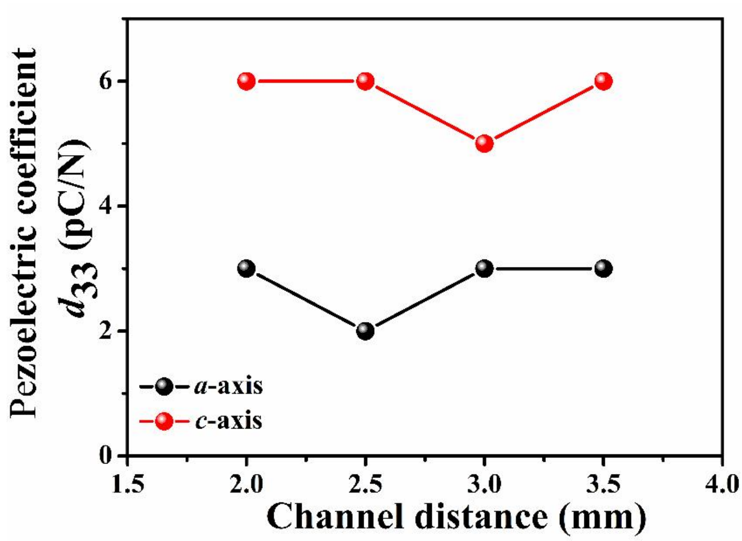

Fig. S6. The piezoelectric response versus channel distance plots for the *a*-axis and *c*-axis.

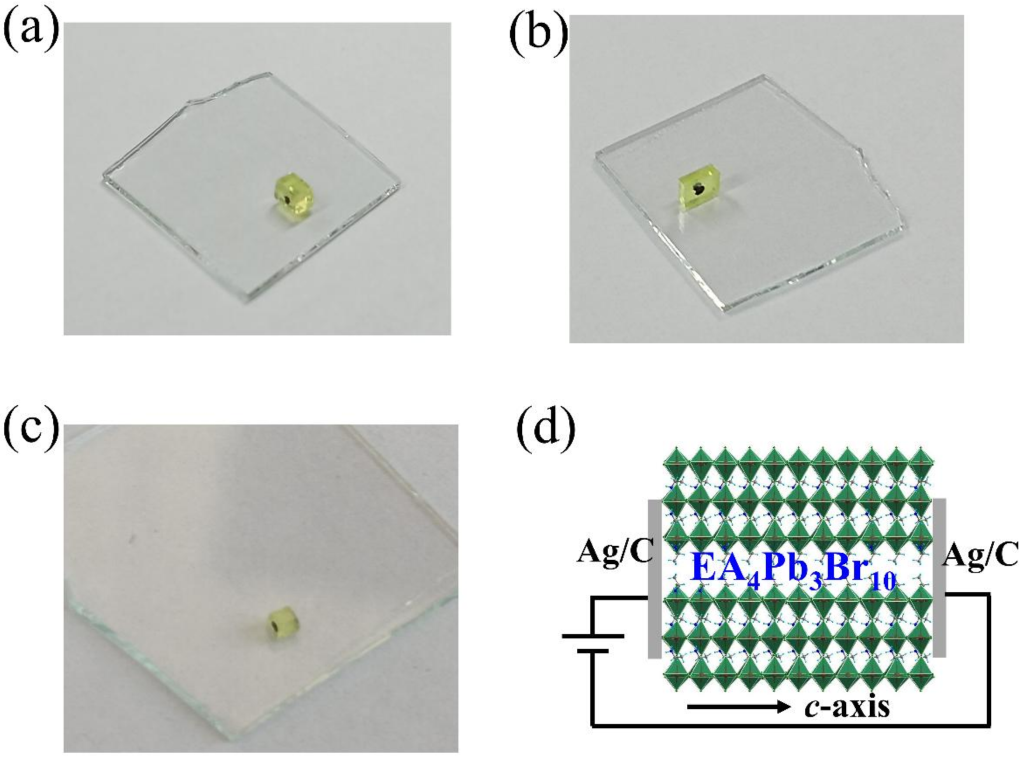

Fig. S7. Photograph of $EA_4Pb_3Br_{10}$ SC devices along the *a*-axis a), *b*-axis b), and *c*-axis c). d) Device Schematic along the *c*-axis.

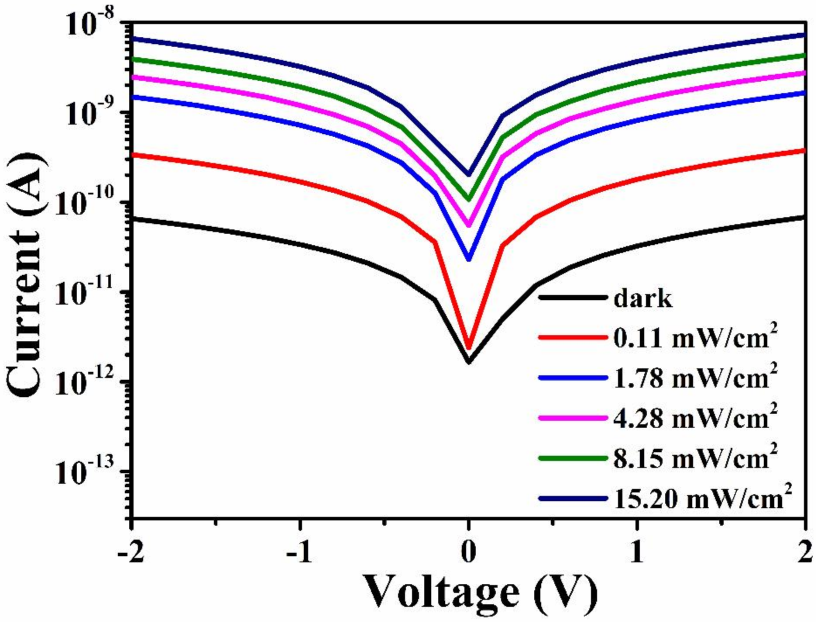

Fig. S8. *I*-*V* curves under various light intensity along the *c*-axes of $EA_4Pb_3Br_{10}$ SC.

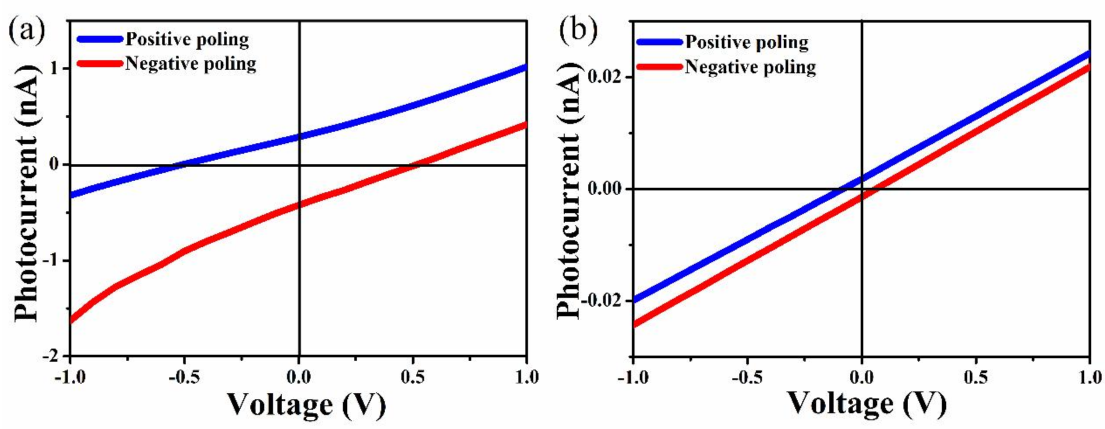

Fig. S9. a) Photocurrent-voltage curves of *c*-direction device after polarization treatment. b) Photocurrent-voltage curves of *b*-direction device in positive and negative polarization states.

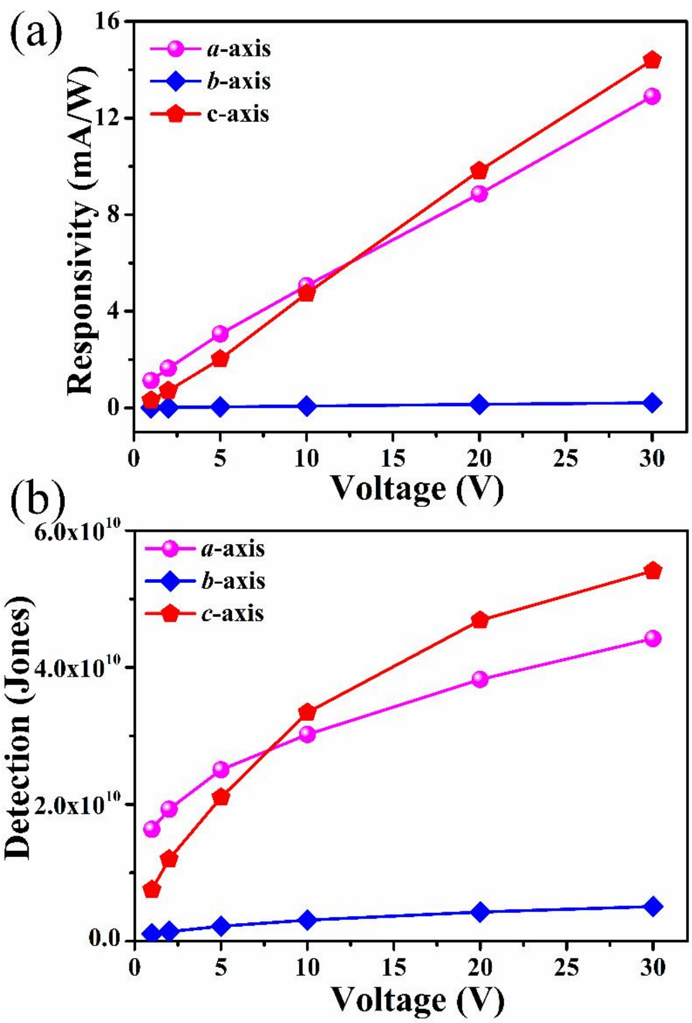

Fig. S10. a) Anisotropic responsivity *R* and b) detection *D** of $EA_4Pb_3Br_{10}$ SCs measured at different bias voltage.

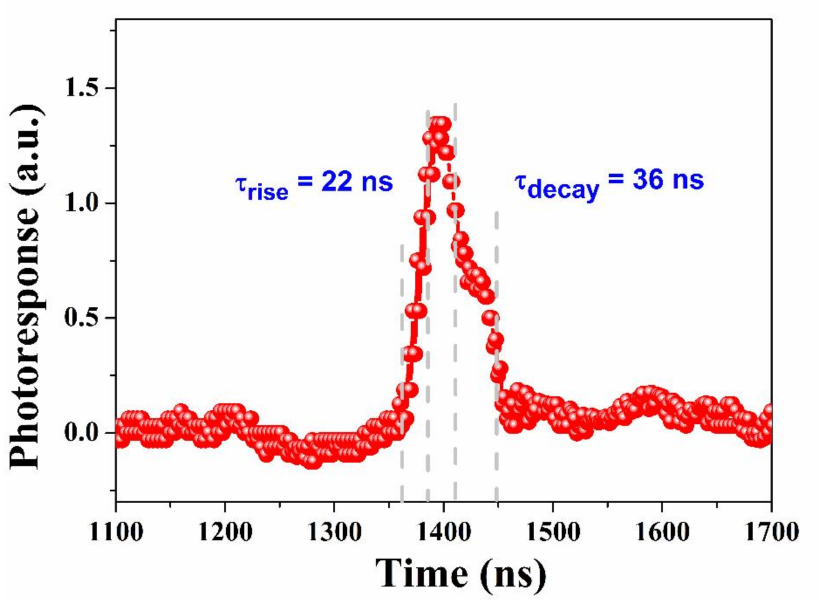

Fig. S11. Transient photoelectric responses under a nanosecond 450 nm laser.

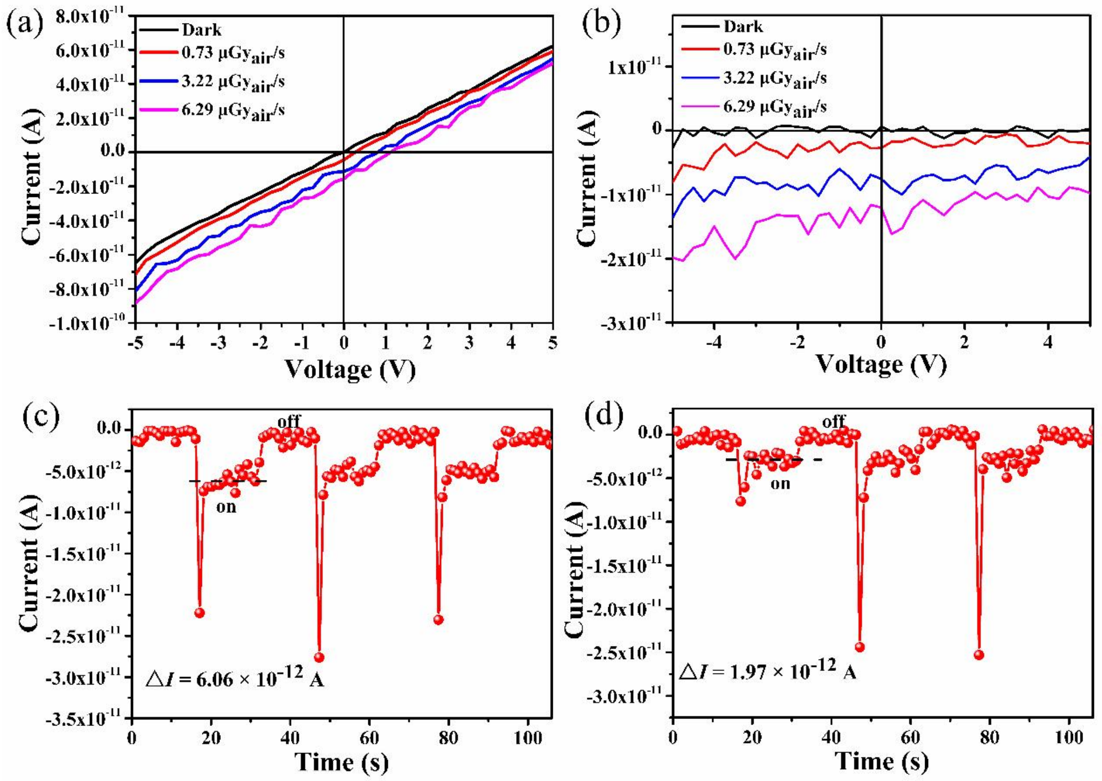

Fig. S12. The *I-V* curves of the *c*-axis detector (a) and the air X-ray detector (b) under various X-ray doses. The X-ray photocurrent responses for the *c*-axis detector (c) and the air X-ray detector (d) under the same dose of 0.73 μGy_{air}/s and 0 V bias.

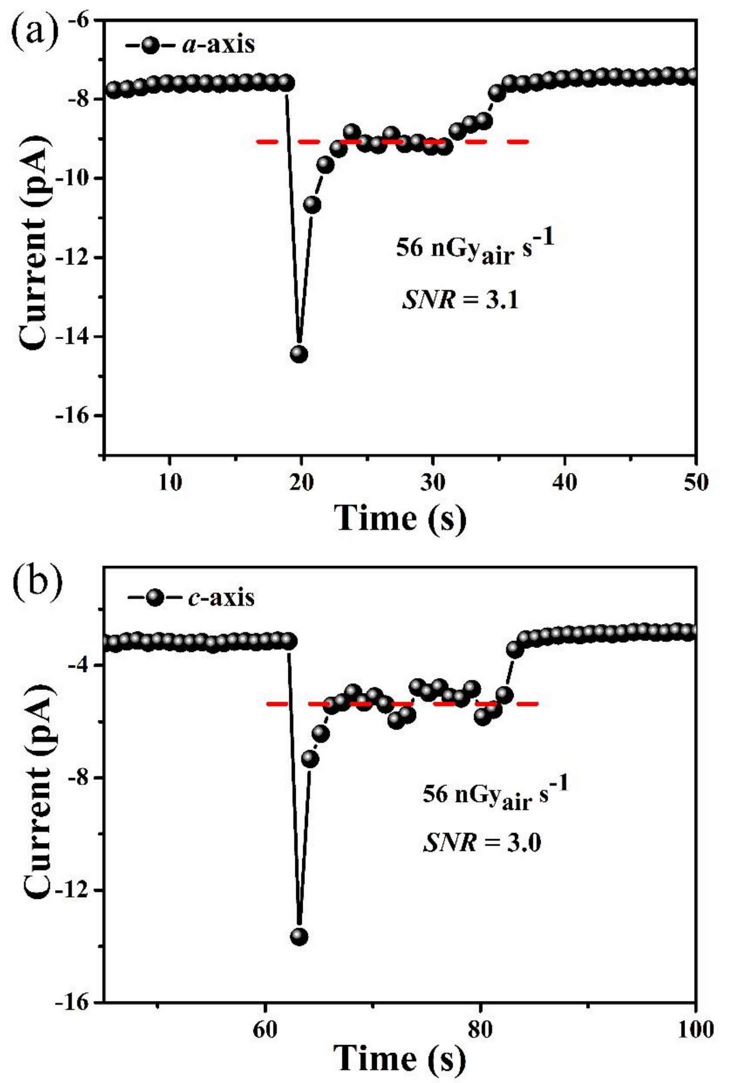

Fig. S13. The X-ray response of *a*-axis (a) and *c*-axis (b) detectors at an ultralow dose of 56 nGy_{air} s^{-1}.

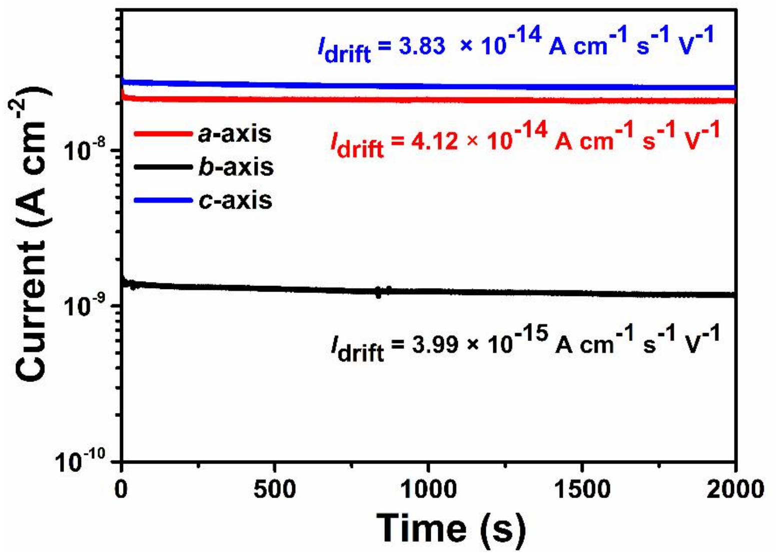

Fig. S14. Comparison of dark current drifts for the *a*-, *b*- and *c*-axes at 2 V bias.

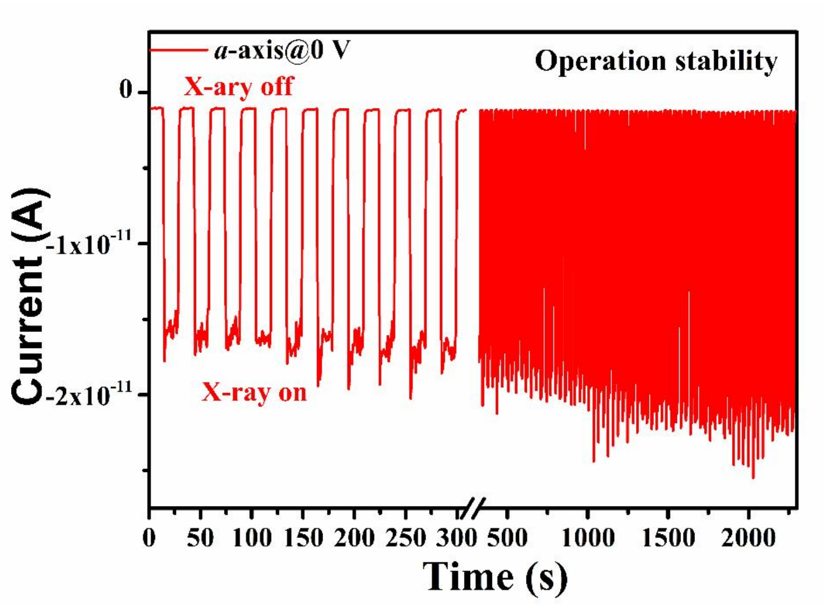

Fig. S15. Operation stability measurement of *a*-axis detector under repeated and continuous X-ray radiation at 0 v bias.

Table S1. Performance comparison of photodetectors based on perovskites.

Devices	λ(nm)	Rise/decay time	Responsivity (mA W^{-1})	Detectivity (Jones)	Condition	Ref.
Si/MAPbBr3/Au	405	520 ns/2435 ns	13.6	5.9×10^{10}	-1 V bias	1
$MAPbI_3$/CdS	700	0.85 ms/2.24 ms	480	2.1×10^{13}	0 V bias	2
Pt/$MAPbBr_3$/Au	350	70 µs/150 µs	2	1.4×10^{11}	0 V bias	3
Au/$(4\text{-TFBMA})_2(DMA)Pb_2I_7$/Au	550	264 µs/380 µs	1.97×10^{3}	2.95×10^{12}	10 V bias	4
Au/$MAPbBr_3$/Au	515	27.6µs/15.8 µs	5.57×10^{4}	8×10^{13}	5 V bias	5
ITO/PEDOT:PSS/$MAPbI_3$/PFN /PM6:Y6/C_{60}/BCP/Ag	860	1.73 µs/ 0.97 µs	577	1.52×10^{13}	0 V bias	6
SWCNT/$CsPbBr_3$/SWCNT	505	13 ms/ 22 ms	1.321×10^{6}	7.7×10^{12}	5 V bias	7
C/$EA_4Pb_3Br_{10}$/C	425	20 ns/ 120 ns	0.22	1.01×10^{10}	0 V (ferroelectric)	This work

1. X. Geng, F. Wang, H. Tian, Q. Feng, H. Zhang, R. Liang, Y. Shen, Z. Ju, G.-Y. Gou, N. Deng, Y.-t. Li, J. Ren, D. Xie, Y. Yang and T.-L. Ren, Ultrafast Photodetector by Integrating Perovskite Directly on Silicon Wafer, *ACS Nano*, 2020, **14**, 2860-2868.
2. F. Cao, L. Meng, M. Wang, W. Tian and L. Li, Gradient Energy Band Driven High-Performance Self-Powered Perovskite/CdS Photodetector, *Adv. Mater.* , 2019, **31**, 1806725.
3. P. A. Shaikh, D. Shi, J. R. D. Retamal, A. D. Sheikh, M. A. Haque, C.-F. Kang, J.-H. He, O. M. Bakr and T. Wu, Schottky junctions on perovskite single crystals: light-modulated dielectric constant and self-biased photodetection, *J. Mater. Chem. C*, 2016, **4**, 8304-8312.
4. W. Guo, H. Chen, X. Liu, Y. Ma, J. Wang, Y. Liu, S. Han, H. Xu, J. Luo and Z. Sun, Rational alloying of secondary and aromatic ammonium cations in a metal-halide perovskite toward crystal-array photodetection, *Sci. China Mater.*, 2021, **65**, 179-185.
5. Y. Liu, Y. Zhang, Z. Yang, J. Feng, Z. Xu, Q. Li, M. Hu, H. Ye, X. Zhang, M. Liu, K. Zhao and S. Liu, Low-temperature-gradient crystallization for multi-inch high-quality perovskite single crystals for record performance photodetectors, *Mater. Today*, 2019, **22**, 67-75.
6. Y. Zhang, Z. Qin, X. Huo, D. Song, B. Qiao and S. Zhao, High-Performance Near-Infrared Photodetectors Based on the Synergy Effect of Short Wavelength Light Filter and Long Wavelength Response of a Perovskite/Polymer Hybrid Structure, *ACS Appl. Mater. Interfaces*, 2021, **13**, 61818-61826.
7. A. A. Marunchenko, M. A. Baranov, E. V. Ushakova, D. R. Ryabov, A. P. Pushkarev, D. S. Gets, A. G. Nasibulin and S. V. Makarov, Single-Walled Carbon Nanotube Thin Film for Flexible and Highly Responsive Perovskite Photodetector, *Adv. Funct. Mater.*, 2022, **32**, 2109834.